

Article

Phase Transformation, Photocatalytic and Photoluminescent Properties of BiPO₄ Catalysts Prepared by Solid-State Reaction: Degradation of Rhodamine B

Abdessalam Bouddouch ^{1,2,3,*}, Elhassan Amaterz ^{1,4} , Bahcine Bakiz ¹, Aziz Taoufyq ¹, Frédéric Guinneton ^{2,3}, Sylvie Villain ^{2,3}, Jean-Raymond Gavarri ^{2,3}, Jean-Christophe Valmalette ^{2,3} and Abdeljalil Benlhachemi ¹ 

¹ Laboratoire Matériaux et Environnement (LME), Faculté des Sciences, Université Ibn Zohr, Agadir 80000, Morocco; amaterzhassan@gmail.com (E.A.); bakizlahcen@gmail.com (B.B.); aziz.taoufyq@gmail.com (A.T.); a.benlhachemi@gmail.com (A.B.)

² Institut Matériaux Microélectronique et Nanosciences de Provence, CNRS, IM2NP, Université de Toulon, 83000 Toulon, France; frederic.guinneton@univ-tln.fr (F.G.); villain@univ-tln.fr (S.V.); jean-raymond.gavarri@univ-tln.fr (J.-R.G.); valmalette@univ-tln.fr (J.-C.V.)

³ Institut Matériaux Microélectronique et Nanosciences de Provence, CNRS, IM2NP, Aix Marseille Université, 13284 Marseille, France

⁴ Institut de Thermique, Mécanique, Matériaux (ITHEMM), Université de Reims Champagne-Ardenne, 51100 Reims, France

* Correspondence: abdo.bouddouch@gmail.com



Citation: Bouddouch, A.; Amaterz, E.; Bakiz, B.; Taoufyq, A.; Guinneton, F.; Villain, S.; Gavarri, J.-R.; Valmalette, J.-C.; Benlhachemi, A. Phase Transformation, Photocatalytic and Photoluminescent Properties of BiPO₄ Catalysts Prepared by Solid-State Reaction: Degradation of Rhodamine B. *Minerals* **2021**, *11*, 1007. <https://doi.org/10.3390/min11091007>

Academic Editor: Keiko Sasaki

Received: 8 July 2021

Accepted: 13 September 2021

Published: 15 September 2021

Publisher's Note: MDPI stays neutral with regard to jurisdictional claims in published maps and institutional affiliations.



Copyright: © 2021 by the authors. Licensee MDPI, Basel, Switzerland. This article is an open access article distributed under the terms and conditions of the Creative Commons Attribution (CC BY) license (<https://creativecommons.org/licenses/by/4.0/>).

Abstract: Polycrystalline bismuth phosphate BiPO₄ was synthesized by solid-state reaction at different temperatures varying from 500 to 900 °C. The samples were characterized by X-ray diffraction (XRD), scanning electron microscopy (SEM), energy dispersive X-ray analysis (EDS) and Raman spectroscopy. The low-temperature phase of BiPO₄ has monoclinic structure with a space group P2₁/n, and was transformed into the monoclinic phase P2₁/m with a slight distortion of monoclinic lattice when it was heated above 500 °C. The effect of the transformation on the structure, morphology and photocatalytic properties was examined. The photocatalytic activity of each sample, in presence of Rhodamine B (RhB) in aqueous solution, was carried out and analyzed under UV light irradiation. Photoexperiments showed that the material prepared at 500 °C is the best catalyst with degradation efficiency of the order of 96% after 12 min of reaction time under UV light irradiation. This high photocatalytic efficiency could be due to their structural and morphological changes. The photocatalytic degradation mechanism of RhB in the presence of the best photocatalyst BiP-500 °C is proposed. The stability of the catalyst was also examined by carrying out four successive tests of the degradation in the presence of BiP-500 °C. Total organic carbon (TOC) was used to further estimate the rate of mineralization in the presence of BiP-500 °C (83% TOC removal). Photoluminescence experiments performed under UV-laser light irradiation revealed emissions in the green-orange range, with optimal intensities for the mix systems observed at 550 °C.

Keywords: bismuth phosphate; solid-state method; monoclinic structure; photocatalytic and photoluminescent properties; degradation mechanism

1. Introduction

The discharge of dye-containing effluents by textile industries is considered as one of the major problems that threatens the aquatic environment [1–3]. In addition to the cosmetic problem, the toxicity and carcinogenic properties of most of these dyes are of serious concern [4,5].

Photocatalysis, as an advanced oxidation process, is considered as one of the best alternatives to deal with this issue. Photocatalysis provides a powerful oxidation via the generation of highly oxidizing species, e.g., radicals OH• [6–9]. These latter are non-selective and can lead to a good removal of all types of non-biodegradable organic contaminants

including dyes, pesticides and pharmaceuticals [10–15]. Unlike conventional techniques, such as the adsorption method on activated carbon or biological treatments, photocatalysis has been considered as a cost-effective method to completely convert organics into CO₂ and H₂O without the production of large quantities of sludge [16–19].

During the last few years, researchers have developed many semiconductors based on oxides [20–23], hydroxides [24,25], tungstates [26–28], molybdates [29] and phosphates [30–38] for the decontamination of wastewater. A good photocatalyst should be simple to prepare, nontoxic, cheap and highly effective in utilizing light for the illumination of organic pollutants [39].

BiPO₄ is a promising photocatalyst material. It has shown a good performance in photoelectrochemical applications such as water splitting and oxidation of organic pollutants. BiPO₄ has three main crystal structures: two monoclinic phases (M₁, space group: P2₁/n and M₂, space group: P2₁/m) and one hexagonal phase (H, space group: P3₁21). Among them, HBIP, with a band gap of 4.6 eV, shows the lowest photocatalytic activity, while M₂ and M₁, with band gaps of 4.2 eV and 3.8 eV, respectively, possess higher photocatalytic activity [40]. M₁ is reported to have much better photocatalytic activity than that of traditional P25 TiO₂ [41–44]. This high photocatalytic activity was explained by the inductive effect of PO₄^{3−} leading to a good separation of the electron and hole pairs [45]. For this reason, BiPO₄-based photocatalysts have been extensively studied for environmental remediation applications [40,46–49].

So far, different methods have been used to synthesize BiPO₄, including the chemical vapor process [50,51], the hydrothermal process [30], microwave synthesis [51] and the sonochemical method [52]. However, the preparation of BiPO₄ materials with controlled phase and morphology is still a challenge for material scientists.

The choice of the synthesis method and the control of the experimental conditions are very important in order to reach the right structural, microstructural, and electrical properties, which are crucial for obtaining the optimum photocatalytic properties to easily degrade organic pollutants. For example, Table 1 summarizes the different preparation methods of BiPO₄ particles with their photocatalytic activities towards the degradation of organic pollutants.

In our recent work [61], BiPO₄ samples were synthesized from polycrystalline precursors obtained by coprecipitation method, then, thermally treated at temperatures Θ of 200, 400, 600 and 900 °C during 3 h. The progressive formation of three polymorphs, hexagonal phase at 200 °C, monoclinic P2₁/n at intermediate temperatures and P2₁/m at 900 °C, allowed observing different behaviors of photocatalytic activities and photoluminescence emissions. The role of thermal decomposition was to modify crystal structures, crystallite dimensions and morphologies to obtain or vary certain properties. The highest photocatalytic efficiencies were observed with large-sized particles of biphasic BiPO₄ samples thermally treated at 400 and 600 °C.

Presently, we develop a systematic study of the photocatalytic and photoluminescent properties of BiPO₄ polymorphs obtained by the traditional solid-state reaction, at different thermal treatment temperatures ranging from 500 to 900 °C.

Table 1. Synthesis methods and photocatalytic properties of BiPO₄.

Methods (Preparation Method/Raw Materials/Optimized Conditions)	Photocatalytic Activity (in Comparison to the Apparent Kinetics Constant k_{app})	Reference
Hydrothermal Reaction/Na ₃ PO ₄ + Bi(NO ₃) ₃ /pH = 1, 180 °C, 96 h	$k_{app} = 0.1225 \text{ min}^{-1}$ for [RhB] = 10 ⁻⁵ M, (UV-254 11 W, cat. 0.5 g/L); as twice as that of P25	[53]
Hydrothermal Reaction/Na ₃ PO ₄ + Bi(NO ₃) ₃ /pH = 1, 180 °C, 72 h	$k_{app} = 0.1839 \text{ min}^{-1}$ for [RhB] = 10 ⁻⁵ M, (UV-254 11 W, cat. 0.5 g/L); as twice as that of P25	[53,54]
Hydrothermal Reaction/Na ₃ PO ₄ + Bi(NO ₃) ₃ /pH = 1, 180 °C, 48 h	$k_{app} = 0.0858 \text{ min}^{-1}$ for [RhB] = 10 ⁻⁵ M, (UV-254 11 W, cat. 0.5 g/L); as twice as that of P25	[53]
Hydrothermal Reaction/Na ₃ PO ₄ + Bi(NO ₃) ₃ /pH = 1, 180 °C, 12 h	$k_{app} = 0.0594 \text{ min}^{-1}$ for [RhB] = 10 ⁻⁵ M, (UV-254 11 W, cat. 0.5 g/L); as twice as that of P25	[53]
Solvothermal reaction/H ₃ PO ₄ + Bi(NO ₃) ₃ + CA-Na/EG-glycerol solution, 120 °C, 20 h	$k_{app} = 0.53 \text{ h}^{-1}$ for [RhB] = 10 ⁻⁵ M and 0.12 h ⁻¹ for 10 ppm MB (UV-254 4 W × 6, cat. 1 g/L)	[55]
Flux/Bi(NO ₃) ₃ + NaH ₂ PO ₄ /pH = 2.2, Bi ³⁺ / PO ₄ ³⁻ = 1:5, 48 h	$k_{app} = 0.193 \text{ min}^{-1}$ (UV-254 11 W, 0.5 g/L, [MB] = 10 ⁻⁵ M;	[56]
Hydrothermal Reaction/NaH ₂ PO ₄ + Bi(NO ₃) ₃ /160 °C, 24 h	$k_{app} = 0.016 \text{ min}^{-1}$ for 50 ppm phenol (UV-254 11 W, cat. 0.5 g/L); Or $k_{app} = 0.036 \text{ min}^{-1}$ by adding 60 ppm H ₂ O ₂	[47]
Microwave synthesis/NaH ₂ PO ₄ + Bi(NO ₃) ₃ /glycerol, EG or DEG aq, 800 W, 15 min	$k_{app} = 0.035 \text{ min}^{-1}$ for 10 mg/L MO (500 W Xe lamp, cat. 1 g/L)	[51]
Hydrothermal reaction/Na ₃ PO ₄ + Bi(NO ₃) ₃ + EDTA/HNO ₃ , 180 °C, 24 h	$k_{app} = 0.0294 \text{ min}^{-1}$ for [MB] = 10 ⁻⁵ M (Xe 500 W, 0.5 g/L, cat. 0.8 g/L)	[57]
Electrospinning method/Bi(NO ₃) ₃ + (NH ₄) ₂ PO ₄ + Citric acid/PVP 0.1 g/mL, pH = 1, Electrospinning voltage 25 kV, speed 1.5 μm/s	$k_{app} = 0.01638 \text{ min}^{-1}$ for 10 ⁻⁵ M APMP pulping effluent (Xe 500 W $\lambda \leq 400 \text{ nm}$, 0.5 g/L, cat. 1.3 g/L) as 3.7 times as that of P25	[48]
Coprecipitation method/Bi(NO ₃) ₃ ·5H ₂ O + NaH ₂ PO ₄ ·2H ₂ O + glycerol – H ₂ O dried at 120 °C for 12 h, calcination in 500 °C for 6 h	$k_{app} = 0.1089 \text{ min}^{-1}$ (UV-254 15 W, 0.5 g/L, [MB] = 3.10 ⁻⁵ M;	[43]
Hydrothermal Reaction/Na ₃ PO ₄ ·12 H ₂ O + Bi(NO ₃) ₃ ·5H ₂ O, 180 °C, 72 h	$k_{app} = 0.071 \text{ min}^{-1}$ for [RhB] = 10 ⁻¹ M (mercury lamp 100 W, cat. 1 g/L)	[58]
Hydrothermal Reaction/Na ₂ HPO ₄ ·12 H ₂ O + Bi(NO ₃) ₃ ·5H ₂ O/pH = 3, 180 °C, 24 h	$k_{app} = 0.001 \text{ min}^{-1}$ for 10 mg/L RhB (500 W Xe lamp, cat. 1.6 g/L)	[59]
Hydrothermal reaction + ultrasonic irradiation (20 kHz)/Na ₃ PO ₄ + Bi(NO ₃) ₃ + HNO ₃ /strong sonicated for 30 min and followed by 180 °C, 24 h	$k_{app} = 0.1589 \text{ min}^{-1}$ for 5 mg/L MB (UV-253.9 10 W Xe lamp, cat. 4 g/L)	[60]

2. Experimental Section

2.1. Reagents

Bismuth oxide (Bi₂O₃) ≥ 99.9% was purchased from Fluka Chemika. Ammonium hydrogen phosphate (NH₄)₂HPO₄ ≥ 98.0% was purchased from ProLabo. The azo dye (Rhodamine B) used in this work was obtained from Sigma-Aldrich. The purity of the dye was greater than 95%. All the reagents were used as received, without further purification.

2.2. Elaboration of Samples

There are several methods for synthesizing phosphate-based materials in powder form. In our previous study concerning BiPO₄ [30,42,53], all samples were obtained from coprecipitation technique followed by thermal treatment at various temperatures [61]. In this work, we developed a new route based on solid-state reaction. BiPO₄ bismuth phosphate was prepared from polycrystalline Bismuth Bi₂O₃ oxide (Fluka Chemika > 99.0%) and ammonium hydrogen phosphate (NH₄)₂HPO₄ (ProLabo ≥ 98.0%). Suitable amounts of these starting precursors were ground in an agate mortar and then thermally heated at different temperatures between 500 and 900 °C with a step of 50 °C for 3 h. The samples presently studied at different temperatures of thermal treatment Θ will be noted BiP-Θ with Θ = 500, 550, 600, 650, 700, 750, 800, 850 and 900 °C.

2.3. Characterization Techniques

The identification of the crystalline powders was carried out by X-ray diffraction (XRD). The XRD patterns of the polycrystalline ceramics were recorded at room temperature using an Empyrean Panalytical diffractometer operating at 45 kV/35 mA, using the CuK(α₁ – α₂) radiation ($\lambda = 1.5406$ and 1.5444 \AA) of copper source with Ni filter, and working in continuous mode with a step size of 0.013°. Scanning electron microscopy (SEM) analysis was used to observe the morphology and the local composition of the crystalline phases. The device used was a Supra 40 VP Column Gemini Zeiss (Zeiss, Iéna, Germany), operated at 20 KeV, coupled with an Energy Dispersive X-rays Spectroscopy

(EDXS) type analyzer, allowing us to determine the local elemental composition of our materials.

Raman spectroscopy was used to correlate the vibrational characteristics with the structural analyses from X-ray diffraction. The Raman spectra were registered at room temperature using spectrometer Horiba Jobin-Yvon HR800 LabRam system, with wavenumbers of Raman shifts ranging between 100 and 1500 cm⁻¹. The 633 nm line of an Ar-ion laser was used as the excitation source; the photonic power applied to the samples was limited to 5 µW with an acquisition time of 30 s.

2.4. Photocatalytic Experiments

The photocatalytic reactor consisted of a light source of 5 UV lamps (Puritec lamp, HNS S 7W (Osram, Berlin, Germany), $\lambda = 254.6$ nm). In the middle of the reactor, the solution to be irradiated was placed in a beaker in which the homogeneity was ensured by a magnetic stirrer. A cooling system was adapted to avoid the effect of temperature. The temperature of the solution was then maintained between 26 ± 1 °C.

The photocatalytic performances of the photocatalysts were evaluated through the photocatalytic degradation of RhB. Each catalyst (mass of 100 mg) was suspended in 100 mL of RhB solution (5 mg L⁻¹). Before irradiation, the solution was stirred for 1 h inside the photoreactor to achieve the adsorption–desorption equilibrium between the catalyst and RhB. During irradiation, 3 mL solutions were collected at times changed from 2 to 30 min depending on the type of photocatalyst. UV visible JENWAY-6705 spectrometry (Cole-Parmer Ltd., Paris, France) was used to determine the variation of concentration of RhB as a function of irradiation time. To propose a degradation mechanism in the presence of the best catalyst, disodium ethylenediaminetetraacetic acid (EDTA-2Na (Sigma-Aldrich, Saint-Louis, Missouri, États-Unis), a scavenger of h⁺), isopropanol (IPA (Sigma-Aldrich, Saint-Louis, Missouri, États-Unis), a scavenger of OH) and L-ascorbic acid (Sigma-Aldrich, Saint-Louis, Missouri, États-Unis), a scavenger of O₂^{•-}) were used. For each test, certain amounts of scavengers (4 mmol L⁻¹) were added into the rhodamine B solution prior to addition of BiPO₄ catalysts. The mineralization of RhB and its intermediates during the photocatalytic reaction was evaluated by the measurement of total organic carbon present in aqueous solution. Analysis was performed with a Shimadzu TOC-5000-A system (Shimadzu, Kyoto, Japan) equipped with a non-dispersive infrared detector (Shimadzu, Kyoto, Japan) and ASI-5000-A auto-sampler (Shimadzu, Kyoto, Japan). The temperature of solution was maintained at 25 ± 4 °C. The photocatalytic efficiency was calculated from the variation of the concentrations of RhB using the intensity Equation (1):

$$\text{Degradation efficiency (\%)} = 100 \times (C_0 - C)/C_0 \quad (1)$$

where C₀ and C are the initial and time t concentrations of RhB, respectively.

2.5. Photoluminescence Experiments

The device used to perform photoluminescence (PL) tests under UV excitation was a Horiba Jobin-Yvon HR800 LabRam spectrometer (Horiba France SAS, Palaiseau, France) equipped with an argon ionized laser, used as an excitation source with a wavelength of 364.8 nm (3.4 eV), and power fixed at 5 µW. The measurements were recorded in the spectral range between 400 and 900 nm with an acquisition time of 5 s.

3. Results and Discussion

3.1. X-ray Diffraction Analyses

Figure 1 depicts the XRD patterns of the as-synthesized BiPO₄ samples obtained by solid-state and calcined at different temperatures changing from 500 to 900 °C. All the detected diffraction peaks for the BiP-500 sample could be indexed into the monoclinic phase with space group P2₁/n (M₁) single phase. When the calcination temperature increases above 550 °C, the nMBIP phase is progressively transformed into the monoclinic phase of BiPO₄ with space group P2₁/m (M₂) (Figure 2). In this instance, I crystal phase

structure of the prepared BiPO_4 samples calcined at $800\text{ }^\circ\text{C}$ exhibits the presence of only a single phase of M_2 . Upon increasing the heat treatment above $850\text{ }^\circ\text{C}$, the appearance of small residues of the M_1 phase is shown. To sum up, $500\text{ }^\circ\text{C}$, $800\text{ }^\circ\text{C}$, and other temperatures give rise to a single phase of M_1 , a single phase of M_2 and a mixture of the two phases.

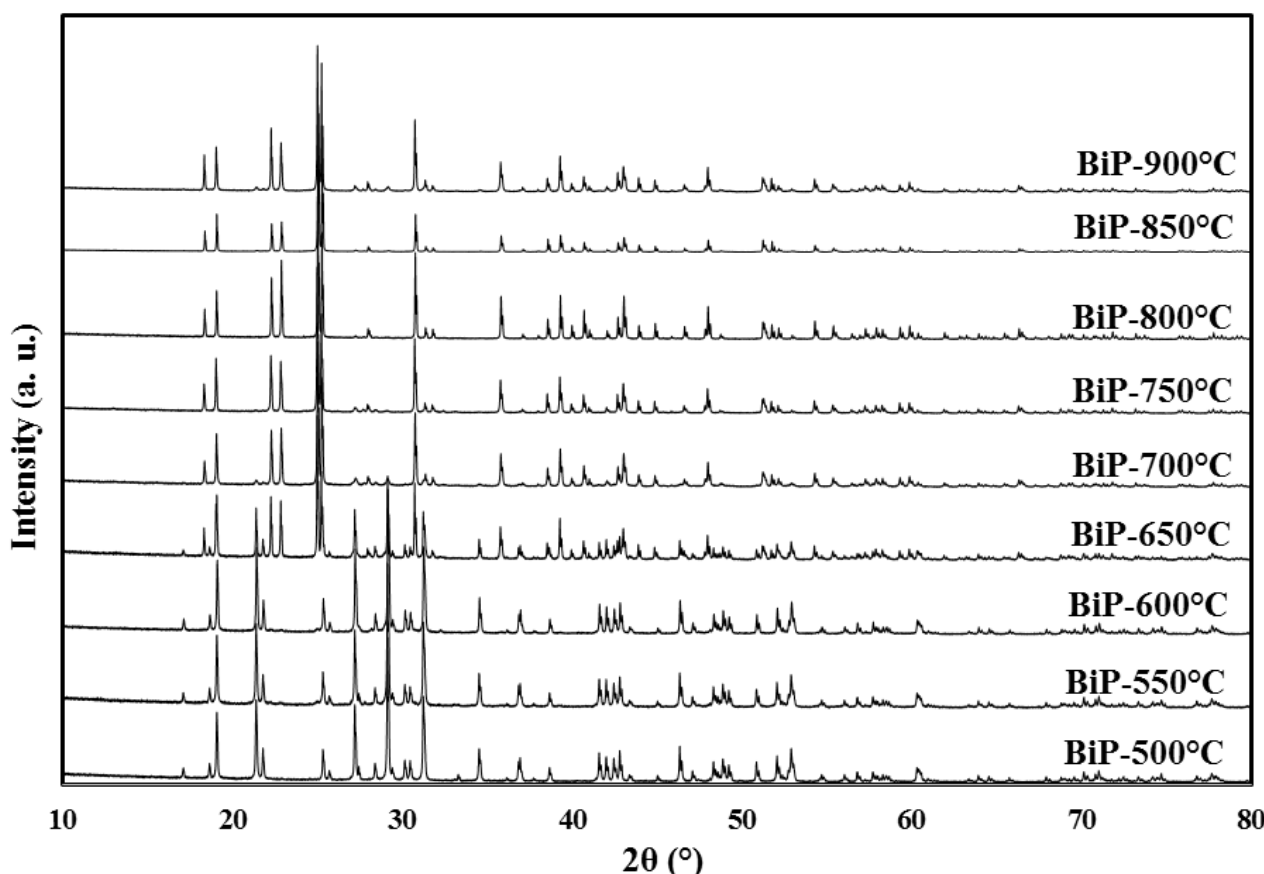


Figure 1. XRD patterns of bismuth phosphate BiPO_4 obtained after different thermal treatments. BiP-500: monoclinic M_1 , at $500\text{ }^\circ\text{C}$; BiP-550 and 600: monoclinic M_1 + traces of monoclinic M_2 , at 550 and $600\text{ }^\circ\text{C}$; BiP-650: monoclinic M_1 + monoclinic M_2 at $650\text{ }^\circ\text{C}$; BiP-800: monoclinic M_2 , at $800\text{ }^\circ\text{C}$; BiP-700, 750, 850 and 900: M_2 + traces of M_1 at 700 , 750 , 850 and 900 .

Based on the intensity of the peaks of the two phases using 'X' Pert High Score Plus software, Version 3.0.5, the portions of the two monoclinic crystal structures of the BiPO_4 samples can be calculated and are depicted in Table 2. As can be seen, calcining the example at $550\text{ }^\circ\text{C}$, a small amount of 9 mol. % of the M_1 was transformed to M_2 . Expanding the calcination temperature, the weight level of M_2 becomes increasingly important until complete vanishing of the M_1 at $800\text{ }^\circ\text{C}$. Above this latter temperature, the opposite is seen; a small amount of the unadulterated M_2 has been transformed into M_1 .

Table 2. The transformed mole fraction of M_1 and M_2 samples sintered at various temperatures.

Calcined Powder	Sintering Temperature ($^\circ\text{C}$)	Weight Fraction	
		M_1	M_2
M_1	500	1	0
	550	0.91	0.09
	600	0.86	0.14
	650	0.44	0.56
	700	0.34	0.66
	750	0.19	0.81
	800	0.02	0.98
M_2	850	0.07	0.93
	900	0.26	0.74

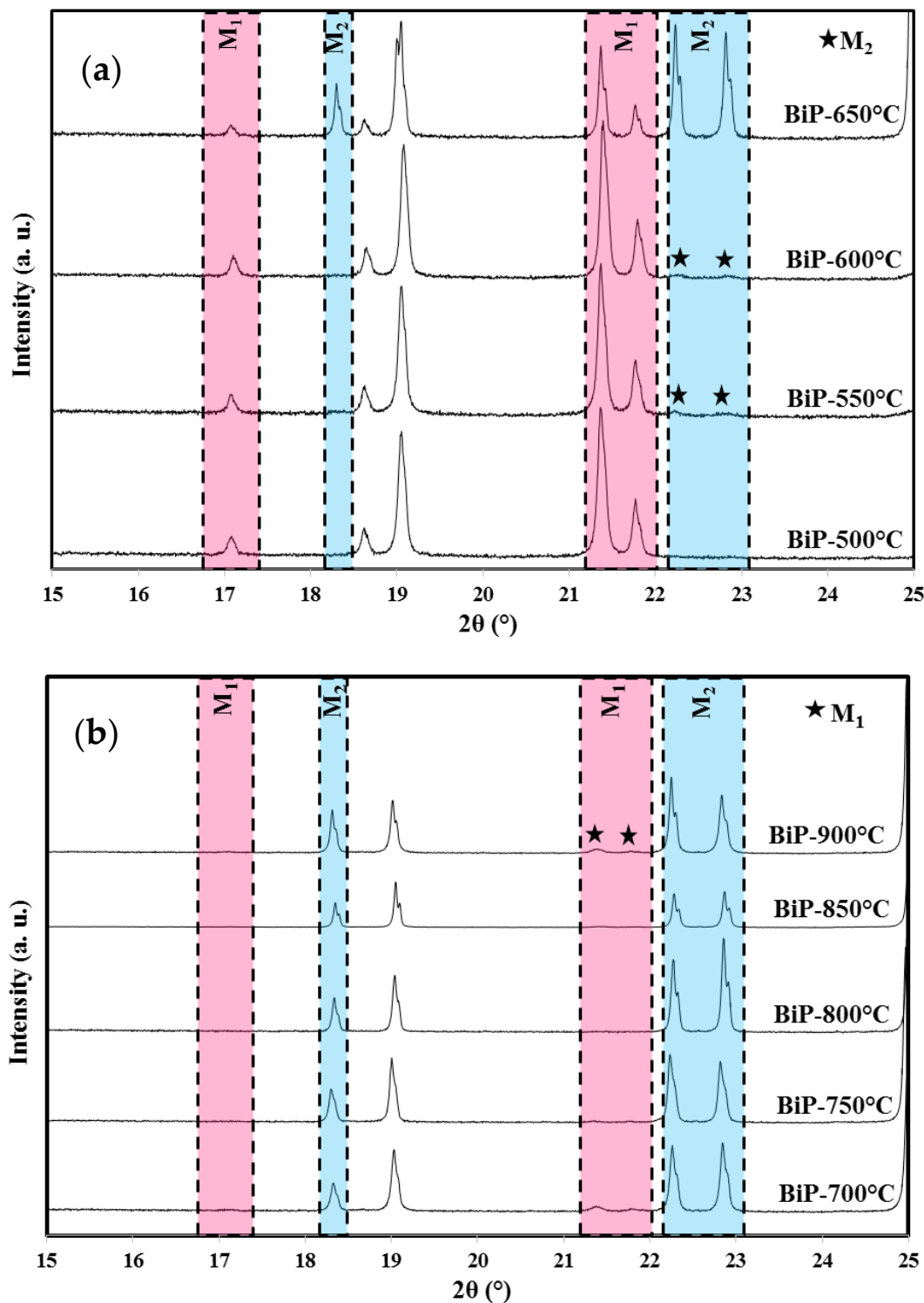


Figure 2. XRD diffraction profiles in the angular range 15° to 25° 2θ of the BiP- Θ samples: the disappearance of the $K\alpha_1-\alpha_2$ doublet of the Bragg peaks for the monoclinic phase M_1 from BiP-700 °C, appearance of the Bragg peaks from BiP-550 °C of the monoclinic phase M_2 . (a) 500, 550, 600 and 650 °C, (b) 700, 750, 800, 850 and 900 °C.

3.2. Scanning Electron Microscopy: Morphology of the Powders

Scanning electron micrographs of the BiPO₄ samples obtained at different calcination temperatures changing from 500 to 900 °C show morphological changes. The BiP-500 and 600 samples (Figure 3a–c) show no significant morphology change with the presence of

spherical particle shapes with 200–300 nm size distributions. A further increase in the calcination temperature from 650 °C to 900 °C dramatically changed the BiPO₄ particles to irregular large particles as they aggregated and bonded with each other to form big clusters (Figure 3d–i). Moreover, it was observed that the initial spherical morphology of BiP-500/600 disappeared, and a new shape with a larger particle size was observed, giving rise to a remarkable decrease in the specific surface areas.

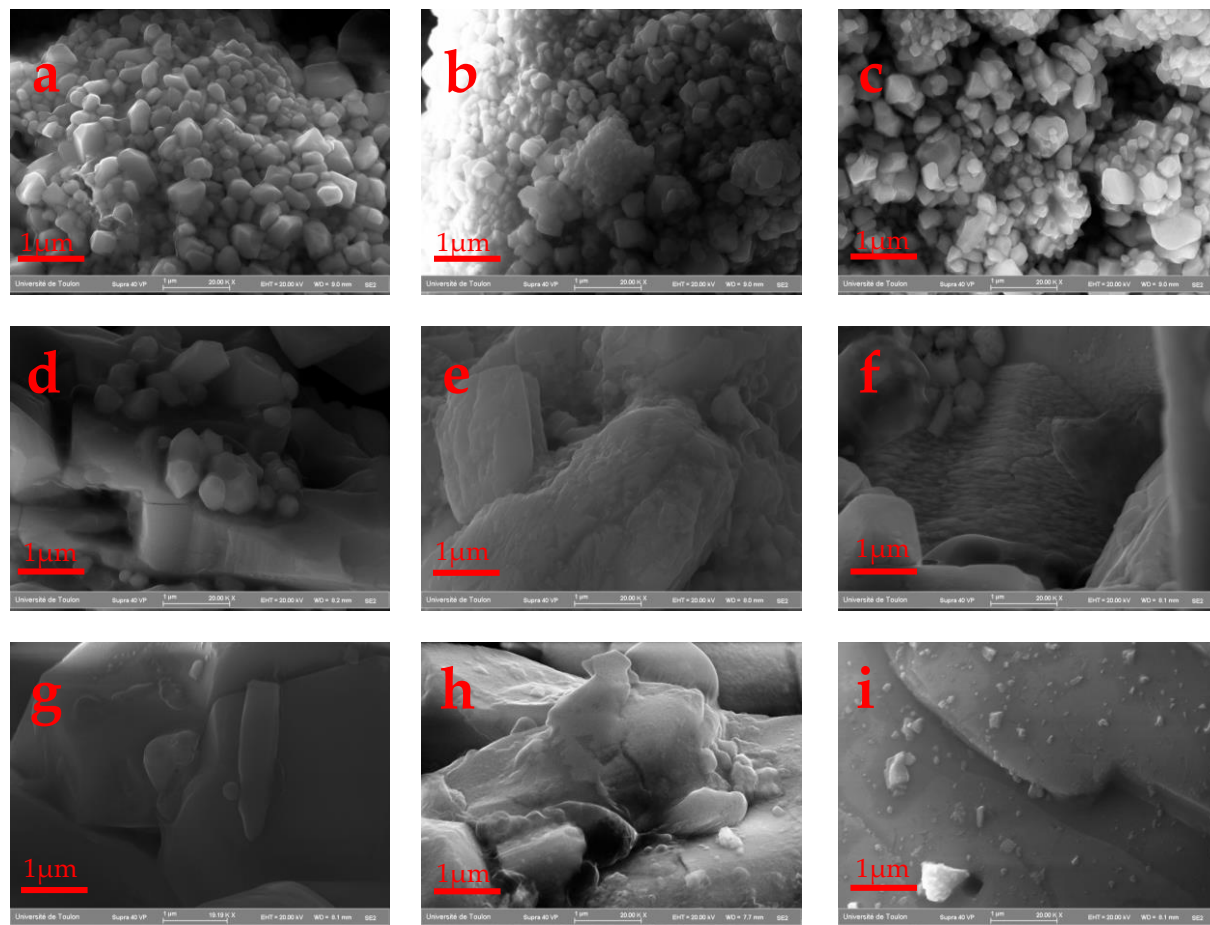


Figure 3. SEM images of: (a) BiP-500, (b) BiP-550, (c) BiP-600, (d) BiP-650, (e) BiP-700 (f) BiP-750, (g) BiP-800, (h) BiP-850 and (i) BiP-900.

From 700 °C to 900 °C, M₂ is the major phase compared to M₁. All samples show a high purity, as the EDX analysis in Table 3 shows. Indeed, the atomic ratio Bi/P is equal to 1 in all the elaborated samples, which further confirms the successful synthesis of BiPO₄.

Table 3. EDX analyses for Bi and P atoms.

Photocatalyst	Atomic Percentage of Bi	Atomic Percentage of P	Experimental Ratio
BiP-500	50.13	49.87	1.005
BiP-550	49.96	50.04	1.001
BiP-600	50.46	49.54	1.010
BiP-650	50.91	49.09	1.037
BiP-700	50.40	49.60	1.016
BiP-750	50.43	49.57	1.017
BiP-800	51.72	48.28	1.071
BiP-850	50.01	49.99	1.000
BiP-900	51.73	48.27	1.071

3.3. Raman Spectroscopy Study

Symmetrical changes of PO_4 tetrahedra with phase transformation during heat treatment were studied using Raman spectroscopy. As shown in Figure 4, some distinct differences can be clearly seen in their vibrational characteristics compared to phosphate groups [62,63]. Based on the group theory analysis, the isolated PO_4 group has a Td symmetry with nine internal modes which can be represented as Equation (2).

$$T_{\text{vib}} = A_1 + E + 2F_2 \quad (2)$$

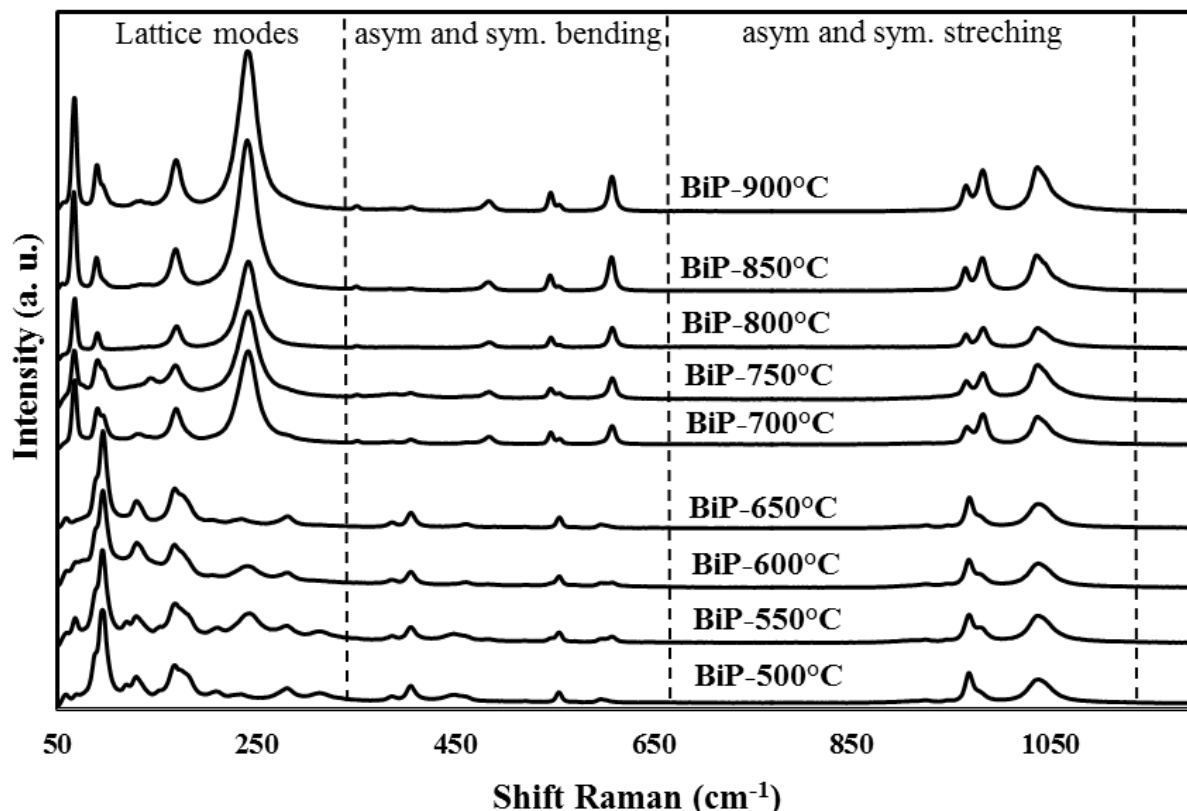


Figure 4. Raman spectra of bismuth phosphate BiPO_4 obtained at different thermal treatments.

It is worth mentioning that the representation E is doubly detached and F_2 is triply detached. The symmetrical (ν_1) and asymmetrical (ν_3) P–O stretching vibrations of the PO_4 group correspond to the A_1 and one mode of F_2 representation, respectively, while the other modes', F_2 and E , representation correspond to the O–P–O flexion of ν_2 and ν_4 , respectively [64,65]. More precisely, the orthophosphate PO_4 group isolated in the monoclinic phase $P2_1/n$ (M_1) is characterized by several bands, such as ν_1 , ν_2 , ν_3 and ν_4 , which are located at 969, 461, 1039 and 597 cm^{-1} , respectively. Depending on the symmetry around the PO_4 phosphate group and the nature of the cation introduced into the matrix, the vibration modes mentioned above undergo a shift either towards blue or towards red. This is the case of the polymorphic change from the monoclinic phase $P2_1/n$ (M_1) to the monoclinic phase $P2_1/m$ (M_2) (Table 4). In other words, the symmetry of the PO_4 phosphate group is changed. More precisely, the experimental values of the wavenumbers for ν_1 , ν_2 , ν_3 and ν_4 are, respectively, 965, 485, 1037 and 609 cm^{-1} [43,64]. In the Raman spectra, the decrease in certain bands and the increase in others show the disappearance of one phase and the disappearance of another, which is confirmed by the fractions of the M_1 and M_2 phases in each sample, which further confirms the results found by X-ray diffraction.

Table 4. Raman spectroscopy data and assignments of vibration bands for the monoclinic phases of BiPO₄.

Raman Data. Wavenumbers in cm ⁻¹ .		
M ₁	M ₂	Assignments
1039	1037	PO ₄ Asym. Stretching. mode ν ₃
	983	
969	965	PO ₄ Sym. Stretching. mode ν ₁
929		
597	609	ν ₄ Bending modes of PO ₄
556	547	
461	485	ν ₂ Bending modes of PO ₄
388	352	
281	242	Bending modes of O–Bi–O
169	169	Stretching vibrations of Bi–O

4. Photocatalytic Properties

To evaluate and compare the photocatalytic activities of the obtained different phases of BiPO₄, the photodecomposition of RhB under UV light irradiation was carried out, and the determination of kinetics constants could be then achieved by following the intensity of the RhB absorption maximal band located at 554 nm.

To determine the kinetic constant, which characterizes the photocatalytic efficiency, a first order kinetics rate law (Langmuir-Hinshelwood model) was proposed as Equation (3) [66]:

$$\ln(C_t/C_0) = -k_{\text{obs}} t \quad (3)$$

Following both the adsorption/desorption (with the catalysts and without UV irradiation) and the photolysis (without the catalysts and under UV irradiation), the BiPO₄ catalysts show only 2% degradation after 12 min of reaction time, which shows that the RhB molecule is stable during this reaction time (Figure 5a).

Figure 5b shows that, under UV irradiation, the intensity of the pollutant absorption band decreases with the irradiation time in the presence of BiPO₄ prepared by solid-state reaction and thermally treated at 500 °C. The position of the maximum of this band is shifted from 554 to about 535 nm during decomposition.

Figure 5c shows the kinetics of photocatalytic degradation in the presence of the various photocatalysts. After 12 min of UV irradiation, the photocatalytic efficiencies determined from the ratio C_t/C₀ of the BiP-Θ catalysts with Θ = 500, 550, 600, 650, 700, 750, 800, 850 and 900 °C reach the values of 96.6%, 78.6%, 69.6%, 50.6%, 24.4%, 14.3%, 17.4%, 21% and 27.7%, respectively. It should be noted that these observed efficiencies result from both photolysis and photocatalysis effects. In other terms, the highest efficiencies should be obtained from sample BiP-500. The results in Figure 5d show that the photocatalytic reaction follows a pseudo-first-order kinetics rate law.

The observed rate constants k_{obs} are reported in Figure 5e. Their values in min⁻¹ are 0.2893, 0.1648, 0.1264, 0.056, 0.0342, 0.0175, 0.0249, 0.025 and 0.0403, for the BiP-Θ photocatalysts with Θ = 500, 550, 600, 650, 700, 750, 800, 850 and 900 °C, respectively.

The photocatalytic efficiencies of the BiPO₄ series produced by solid–solid reaction, and, in particular, the high photocatalytic efficiency of the BiP-500 phase obtained at 500 °C, appear to be the highest of the series studied, the rate constants being at least 15 times stronger than those of the other photocatalysts, especially compared to BiP-750.

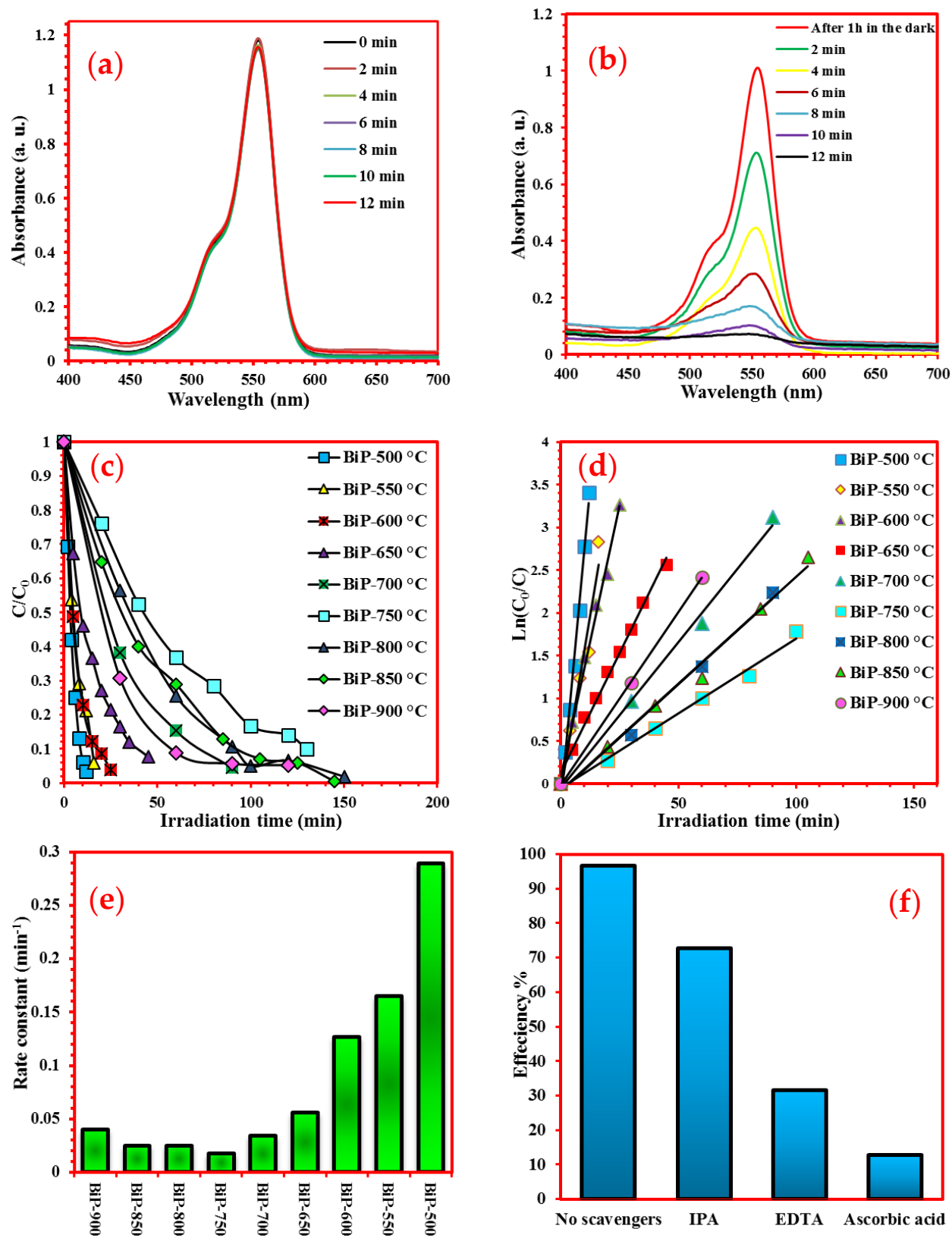


Figure 5. (a) Stability of RhB under UV light; (b) UV-vis absorption with time irradiation of a solution containing 100 mg of BiP-500 °C and 5 ppm RhB; (c) Degradation efficiencies of the as-prepared samples; (d) Pseudo-first-order kinetics of the photocatalysts; (e) Evolution of the apparent rate constant k as function of photocatalysts; (f) Effect of scavengers on the photocatalytic degradation of RhB by BiP-500.

These improved efficiencies could be correlated to the observed specific morphologies characterized by well-crystallized small-sized grains, and also to the presence of the monoclinic phase with space group P2₁/n [67,68]. It is worth mentioning that the photocatalytic properties of the obtained samples decrease as a function of the heat treatment; therefore, these results are in a good agreement with the XRD and SEM results. Indeed, the M₁ amount decreases while that of M₂ increases; this latter shows less activity towards RhB degradation, which explains the obtained results.

As we have mentioned above, the photocatalytic degradation of RhB was studied in an aqueous suspension of bismuth phosphates. The discoloration of this pollutant in the presence of the best photocatalyst (BiP-500 °C) is total after 12 min of UV irradiation at an initial concentration of 5 mg·L⁻¹. In order to determine the photocatalytic mechanism and to confirm the main active species in the photocatalytic process, such as hydroxyl radical (OH[•]), hole (h⁺) and superoxide radical (O₂^{•-}), active species trapping experiments were carried out. More precisely, the photocatalytic degradation of RhB in the presence of scavengers has been studied. Isopropanol alcohol (IPA), disodium ethylenediaminetetraacetic acid (EDTA-2Na) and L-ascorbic acid were used as scavengers of (OH[•]) species, holes (h⁺) and (O₂^{•-}) species, respectively.

The removal efficiency of RhB onto BiP-500 in the presence of different scavengers (L-ascorbic acid, EDTA-2Na, and IPA) is shown in Figure 5f. The photocatalytic degradation efficiency of RhB is 96.6% in the absence of any scavenger. L-ascorbic acid, EDTA-2Na significantly decrease the degradation of RhB with efficiencies of 12.8% and 31.6%, respectively. We obtained a degradation rate of 72.7% in the presence of IPA. These results, therefore, show that the degradation process is enhanced predominantly by holes (h⁺) and superoxide radicals (O₂^{•-}). The hydroxyl radical plays a minor role in the degradation mechanism since the efficiency of the degradation of was not decreased in a significant way when this radical was inhibited. We can assume that the degradation of RhB can be summarized in the following reactions:

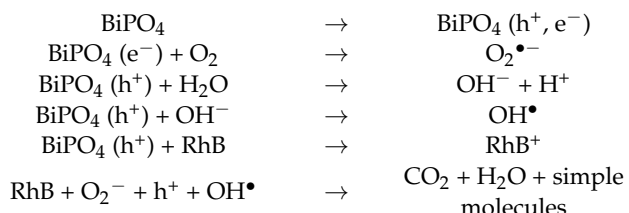


Figure 6 shows the total organic carbon (TOC) removal efficiency using BiP-500 has attained about 83% after 12 min under UV-visible light irradiation. This shows that BiP-500 exhibits important photocatalytic performance for the photodegradation of RhB. Such results also demonstrate that the RhB would be mineralized into CO₂ and H₂O by the as-prepared samples, which is in favor of its application in the field of the treatment of wastewater.

Stability of the BiP-500 °C Catalyst

The photostability and reusability of the photocatalyst activity during the depollution process is an important parameter to consider from an economical point of view. Thus, in order to verify the efficiency of the recycling of the photocatalyst used in this work, four recycling tests were carried out. The sample can be separated easily after each cycle of the photocatalysis reaction. The results of photostability are shown in Figure 7. The initial concentration of RhB was set at 0.01 mmol L⁻¹ in the presence of 100 mg of the catalyst.

For each test, irradiation was carried out for 12 min under UV-visible. After repeating the process four times, the photocatalytic activity slightly decreased from 96% to 82%; this slight decrease may be due to the decrease in catalyst mass and the deactivation of some active sites of our catalyst by the organic pollutant. These results indicate the high stability and reusability of our photocatalyst.

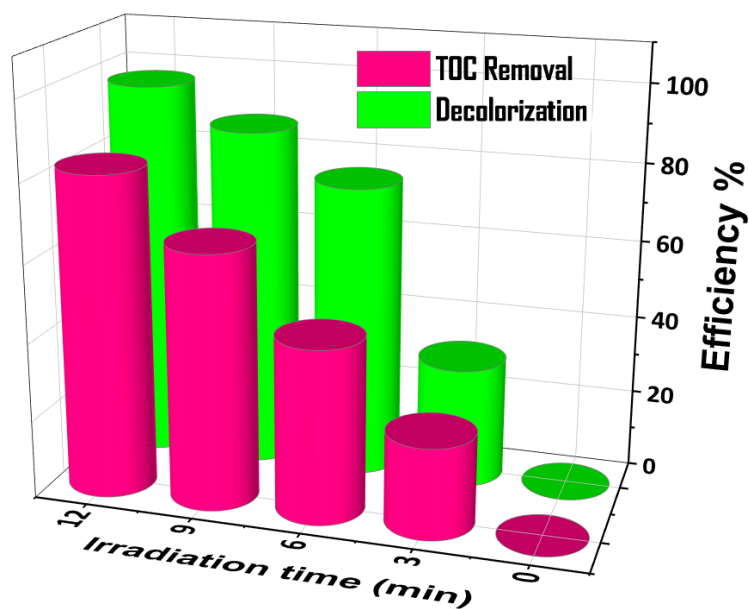


Figure 6. TOC removal vs. discoloration of Rhodamine B over as BiP-500 photocatalyst.

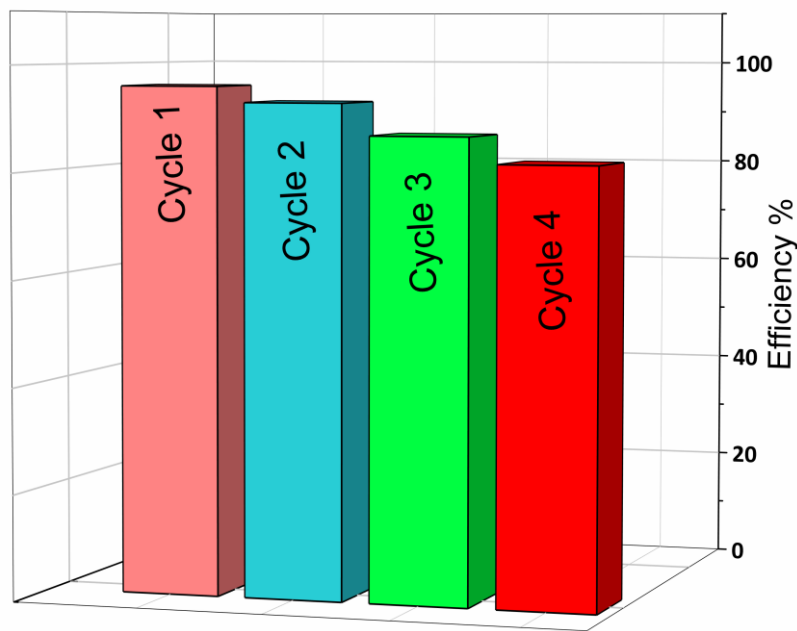


Figure 7. Discoloration performance of recycled catalyst ($[RhB] = 0.01\text{ mM}$; irradiation time = 12 min; [Catalyst] = 1.0 g/L; room temperature).

5. Photoluminescent Properties

The photoluminescence spectra of BiP- Θ materials were recorded under UV excitation and are shown in Figure 8a,b. These emission spectra were processed using the LabSpec program. The broad emission bands observed in the range 400 to 800 nm in all the powders of the BiP- Θ samples with $\Theta = 500, 550, 600, 650$ and $700\text{ }^{\circ}\text{C}$ (Figure 8a), show similar profiles with a maximum at $515 \pm 20\text{ nm}$. The results in the literature have shown that, in the case of Bi^{3+} isolated in a solid matrix, the allowed transition of Bi^{3+} is ${}^3\text{P}_1 \rightarrow {}^1\text{S}_0$, and that it is characterized by emission spectra with wavelengths close to 470 nm (2.6 eV) [61]. In the case of the study of the three polymorphic varieties of BiPO_4 , the Bi^{3+} emissions under excitation at 360 nm were observed at 450 nm (2.8 eV) for the hexagonal and monoclinic

M_1 phases. Currently, a wide emission band (450 to 700 nm) is systematically observed: the emission profile can be broken down into several emissions comprising at least three components (470, 510–520 and 600–680 nm). Emissions ranging from 500 nm to 700 nm are generally attributed to surface defects. This was also the case for BiPO_4 prepared by the coprecipitation method, where a similar broad band was bound to the M_1 structure and attributed to transitions associated with changes in Bi^{3+} environments, due to the presence of oxygen vacancy defects $[\text{V}_O]^{q^\circ}$ (where q° is the positive electric charge with $q = 0, 1$ or 2) disrupting the PO_4 and BiO_8 structural groups of the monoclinic structure. Other defects could also be at the origin of this broadband (Bi vacancies or interstitial sites).

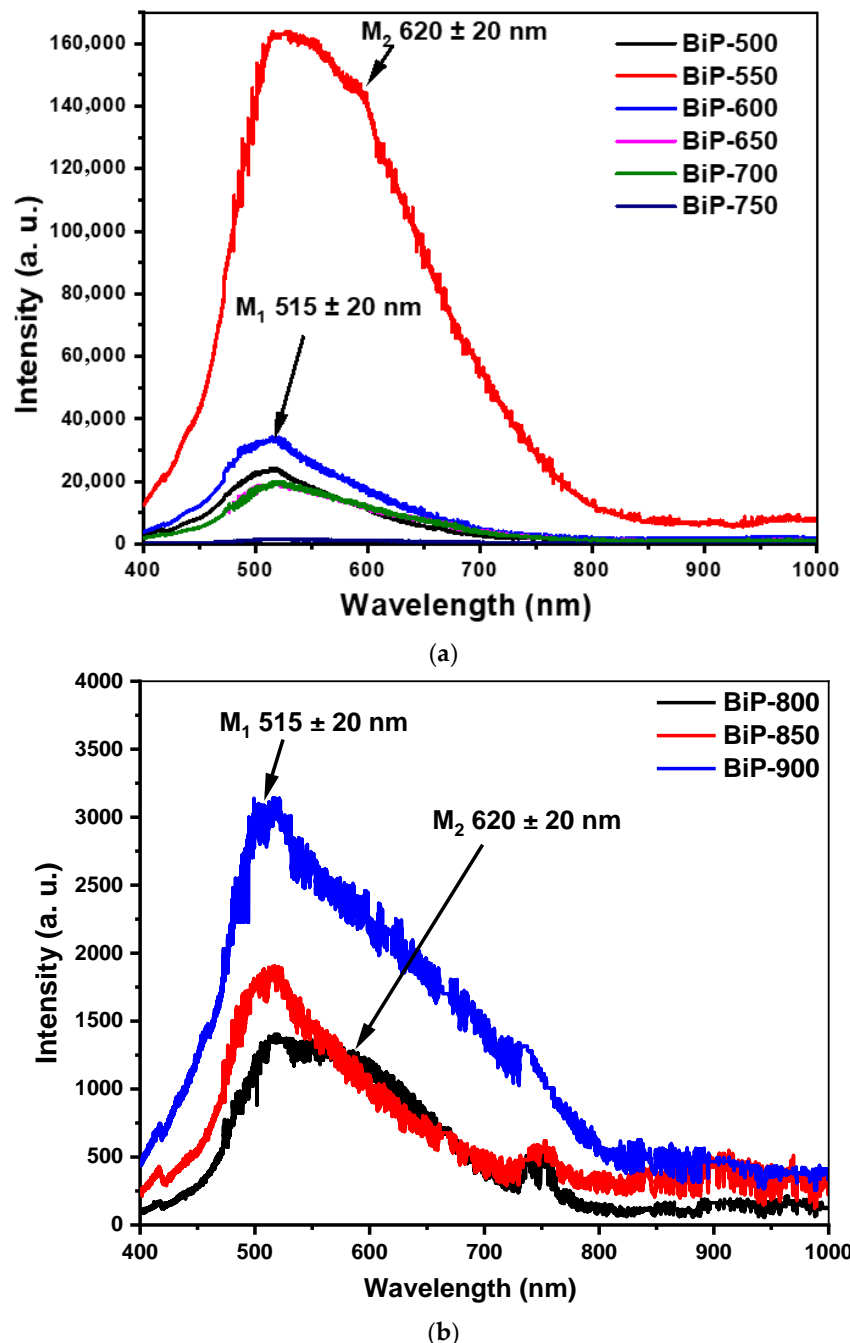


Figure 8. UV-excited photoluminescence spectra (364 nm) of BiPO_4 prepared by solid state reaction and heat treated at (a) 500, 550, 600, 650, 700 and 750 $^{\circ}\text{C}$, (b) 800, 850 and 900 $^{\circ}\text{C}$.

The BiP-750 sample, which was characterized by the presence of the majority of the monoclinic M_2 phase, showed a single band with a maximum close to $(620 \pm 20 \text{ nm})$. In the case of the BiP- Θ samples with $\Theta = 800, 850$ and $900 \text{ }^\circ\text{C}$ (Figure 8b), two characteristic bands of phase M_1 ($515 \pm 20 \text{ nm}$) and M_2 ($620 \pm 20 \text{ nm}$) were observed, with low intensities compared to the other BiP- Θ samples with $\Theta = 500, 550, 600, 650$ and $700 \text{ }^\circ\text{C}$.

In Figure 9, we have reported the intensities of the maximum bands as a function of the heat treatment temperature Θ . The two characteristic bands of phase M_1 ($515 \pm 20 \text{ nm}$) and M_2 ($620 \pm 20 \text{ nm}$) show almost invariant intensities with Θ . We observed a maximum for the polymorph sample BiP-550 (M_1 and traces of M_2). The intensity observed for this particular sample is more than five times greater than that observed for the pure phase BiP-500 (monoclinic M_1) and one hundred times greater than that of BiP-750 and BiP-800 (monoclinic M_2). These results of photoluminescence under UV (364 nm) are in good agreement with the results of the characterization of powders by XRD, more precisely according to the appearance and disappearance of the two monoclinic phases, M_1 and M_2 .

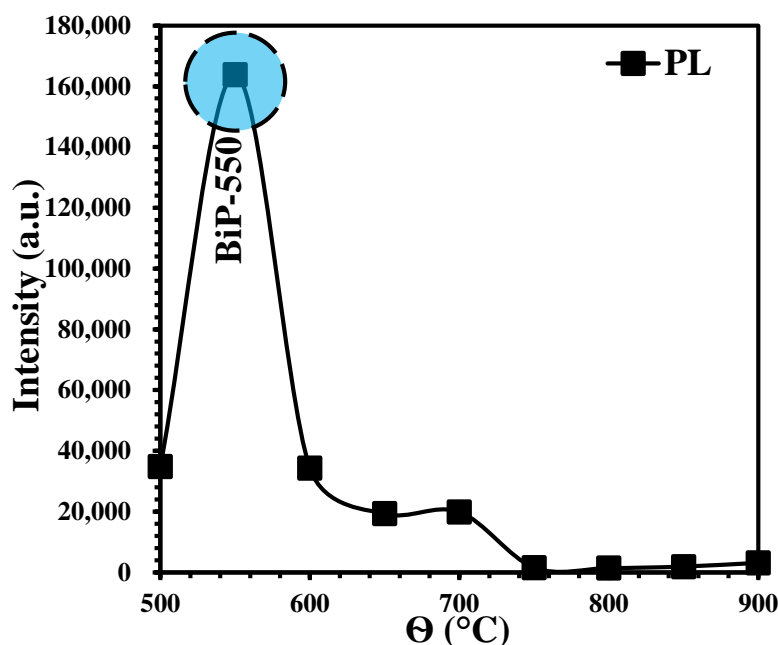


Figure 9. Variation of intensity of BiP- Θ samples with elaboration temperature.

6. Conclusions

The phase change and photocatalytic properties of BiPO_4 ceramics were examined. The monoclinic phase of BiPO_4 with space group $P2_1/n$ (phase stable at low-temperature) was transformed into the monoclinic phase with space group $P2_1/m$ (phase stable at high-temperature) when it was heated above $500 \text{ }^\circ\text{C}$. When the low-temperature phase was thermally heated at $800 \text{ }^\circ\text{C}$, the pure phase M_2 was obtained perfectly. From heat treatment at 850 to $900 \text{ }^\circ\text{C}$ of M_2 , a small fraction of M_2 was transformed into M_1 again. From a quantitative analysis based on the relative intensities of the two-phase mixture, the amount of transformed phase was calculated and the photocatalytic properties of BiPO_4 ceramics with the variation of the fraction of the two phases were studied. The best photocatalytic activity was obtained with the BiP-500/600/650 samples corresponding to the $P2_1/n$ phase and presenting the smallest grain sizes. The mechanism of photocatalytic degradation and the stability of the best photocatalyst towards the degradation of RhB as a polluting dye have been studied. The mineralization of the pollutant studied in the presence of our photocatalyst was confirmed by carrying out TOC tests.

Author Contributions: A.B. (Abdessalam Bouddouch): Investigation, Writing—original draft, Methodology; E.A.: Discussion, Data curation; B.B.: Supervision, Writing—review and editing; A.T.: Writing—

review and editing; F.G.: Supervision, Characterization; S.V.: Supervision, Characterization; J.-R.G.: review and editing; J.-C.V.: Characterization and Data Curation; A.B. (Abdeljalil Benlhachemi): Supervision, Conceptualization. All authors have read and agreed to the published version of the manuscript.

Funding: Financially supported by CAMPUS FRANCE (PHC TOUBKAL 2018 (France–Morocco bilateral program) Grant Number: 38999WE) and PPR project financed by the CNRST under number PPR/2015/32.

Acknowledgments: This work was carried out in the laboratory materials and environment (LME), at the faculty of sciences Agadir, Ibn Zohr University, IM2NP laboratory, University of Toulon.

Conflicts of Interest: The authors declare that they have no known competing financial interests or personal relationships that could have appeared to influence the work reported in this paper.

References

1. Al-Mamun, M.; Kader, S.; Islam, M.; Khan, M. Photocatalytic activity improvement and application of UV-TiO₂ photocatalysis in textile wastewater treatment: A review. *J. Environ. Chem. Eng.* **2019**, *7*, 103248. [[CrossRef](#)]
2. Tounsiadi, H.; Metarfi, Y.; Taleb, M.; El Rhazi, K.; Rais, Z. Impact of chemical substances used in textile industry on the employee's health: Epidemiological study. *Ecotoxicol. Environ. Saf.* **2020**, *197*, 110594. [[CrossRef](#)]
3. Haounati, R.; Ouachtk, H.; El Haouti, R.; Akhouairi, S.; Largo, F.; Akbal, F.; Benlhachemi, A.; Jada, A.; Addi, A.A. Elaboration and properties of a new SDS/CTAB@Montmorillonite organoclay composite as a superb adsorbent for the removal of malachite green from aqueous solutions. *Sep. Purif. Technol.* **2020**, *255*, 117335. [[CrossRef](#)]
4. Chennah, A.; Naciri, Y.; Taoufyq, A.; Bakiz, B.; Bazzi, L.; Guinneton, F.; Villain, S.; Gavarri, J.R.; Benlhachemi, A. Electrodeposited zinc phosphate hydrate electrodes for electrocatalytic applications. *J. Appl. Electrochem.* **2018**, *49*, 163–177. [[CrossRef](#)]
5. Naciri, Y.; Hsini, A.; Ajmal, Z.; Bouddouch, A.; Bakiz, B.; Navío, J.; Albourine, A.; Valmalette, J.-C.; Ezahri, M.; Benlhachemi, A. Influence of Sr-doping on structural, optical and photocatalytic properties of synthesized Ca₃(PO₄)₂. *J. Colloid Interface Sci.* **2020**, *572*, 269–280. [[CrossRef](#)]
6. Bouddouch, A.; Amaterz, E.; Taoufyq, A.; Bakiz, B.; Guinneton, F.; Villain, S.; Valmalette, J.; Gavarri, J.; Benlhachemi, A. Photocatalytic and photoluminescent properties of a system based on SmPO₄ nanostructure phase. *Mater. Today Proc.* **2020**, *27*, 3139–3144. [[CrossRef](#)]
7. Souza, R.P.; Ambrosio, E.; Souza, M.T.F.; Freitas, T.K.F.S.; Ferrari-Lima, A.M.; Garcia, J.C. Solar photocatalytic degradation of textile effluent with TiO₂, ZnO, and Nb₂O₅ catalysts: Assessment of photocatalytic activity and mineralization. *Environ. Sci. Pollut. Res.* **2017**, *24*, 12691–12699. [[CrossRef](#)]
8. Maleki, A.; Safari, M.; Shahmoradi, B.; Zandsalimi, Y.; Daraei, H.; Gharibi, F. Photocatalytic degradation of humic substances in aqueous solution using Cu-doped ZnO nanoparticles under natural sunlight irradiation. *Environ. Sci. Pollut. Res.* **2015**, *22*, 16875–16880. [[CrossRef](#)]
9. Frederichi, D.; Scaliante, M.H.N.O.; Bergamasco, R. Structured photocatalytic systems: Photocatalytic coatings on low-cost structures for treatment of water contaminated with micropollutants—A short review. *Environ. Sci. Pollut. Res.* **2021**, *28*, 23610–23633. [[CrossRef](#)]
10. Herrmann, J.-M. Heterogeneous photocatalysis: State of the art and present applications In honor of Pr. R.L. Burwell Jr. (1912–2003), Former Head of Ipatieff Laboratories, Northwestern University, Evanston (Ill). *Top. Catal.* **2005**, *34*, 49–65. [[CrossRef](#)]
11. Im, J.-K.; Son, H.-S.; Kang, Y.-M.; Zoh, K.-D. Carbamazepine Degradation by Photolysis and Titanium Dioxide Photocatalysis. *Water Environ. Res.* **2012**, *84*, 554–561. [[CrossRef](#)]
12. Chi, C.; Pan, J.; You, M.; Dong, Z.; Zhao, W.; Song, C.; Zheng, Y.; Li, C. The porous TiO₂ nanotubes/Ag₃PO₄ heterojunction for enhancing sunlight photocatalytic activity. *J. Phys. Chem. Solids* **2018**, *114*, 173–178. [[CrossRef](#)]
13. Farbod, M.; Khademalrasool, M. Synthesis of TiO₂ nanoparticles by a combined sol-gel ball milling method and investigation of nanoparticle size effect on their photocatalytic activities. *Powder Technol.* **2011**, *214*, 344–348. [[CrossRef](#)]
14. Radwan, E.K.; Yu, L.; Achari, G.; Langford, C.H. Photocatalytic ozonation of pesticides in a fixed bed flow through UVA-LED photoreactor. *Environ. Sci. Pollut. Res.* **2016**, *23*, 21313–21318. [[CrossRef](#)] [[PubMed](#)]
15. Amaterz, E.; Tara, A.; Bouddouch, A.; Taoufyq, A.; Bakiz, B.; Benlhachemi, A.; Jbara, O. Photo-electrochemical degradation of wastewaters containing organics catalysed by phosphate-based materials: A review. *Rev. Environ. Sci. Bio/Technol.* **2020**, *19*, 843–872. [[CrossRef](#)]
16. Fu, H.; Pan, C.; Yao, A.W.; Zhu, Y. Visible-Light-Induced Degradation of Rhodamine B by Nanosized Bi₂WO₆. *J. Phys. Chem. B* **2005**, *109*, 22432–22439. [[CrossRef](#)]
17. Hoffmann, M.R.; Martin, S.T.; Choi, W.; Bahnemann, D.W. Environmental Applications of Semiconductor Photocatalysis. *Chem. Rev.* **1995**, *95*, 69–96. [[CrossRef](#)]
18. Haounati, R.; El Guerdaoui, A.; Ouachtk, H.; El Haouti, R.; Bouddouch, A.; Hafid, N.; Bakiz, B.; Santos, D.; Taha, M.L.; Jada, A.; et al. Design of direct Z-scheme superb magnetic nanocomposite photocatalyst Fe₃O₄/Ag₃PO₄@Sep for hazardous dye degradation. *Sep. Purif. Technol.* **2021**, *277*, 119399. [[CrossRef](#)]

19. Ellouzi, I.; Bouddouch, A.; Bakiz, B.; Benlhachemi, A.; Oualid, H.A. Glucose-assisted ball milling preparation of silver-doped biphasic TiO_2 for efficient photodegradation of Rhodamine B: Effect of silver-dopant loading. *Chem. Phys. Lett.* **2021**, *770*, 138456. [[CrossRef](#)]
20. Jan, T.; Azmat, S.; Wahid, B.; Adil, M.; Alawadhi, H.; Mansoor, Q.; Farooq, Z.; Ilyas, S.; Ahmad, I.; Ismail, M. Chemically synthesized $\text{ZnO-Bi}_2\text{O}_3$ (BZO) nanocomposites with tunable optical, photoluminescence and antibacterial characteristics. *Mater. Sci. Semicond. Process.* **2018**, *84*, 71–75. [[CrossRef](#)]
21. Bao, N.; Liu, Y.; Li, Z.-W.; Yu, H.; Bai, H.-T.; Xia, L.; Feng, D.-W.; Zhang, H.-B.; Dong, X.-T.; Wang, T.-Y.; et al. Construction of order mesoporous (Eu-La)/ZnO composite material and its luminescent characters. *J. Lumin.* **2016**, *177*, 409–415. [[CrossRef](#)]
22. Ajmal, M.; Ali, T.; Mian, S.A.; Khan, M.A.; Ahmad, S.; Khan, A.A. Effects of Ce^{3+} -doping concentration on the luminescent properties of La_2O_3 : Ce^{3+} phosphors. *Mater. Today Proc.* **2017**, *4*, 4924–4929. [[CrossRef](#)]
23. Amaterz, E.; Bouddouch, A.; Tara, A.; Taoufyq, A.; Bakiz, B.; Benlhachemi, A.; Jbara, O. Correlation between photoluminescence and photoelectrochemical properties of $\text{SrHPO}_4/\text{BaHPO}_4/\text{FTO}$ anode material. *Opt. Mater.* **2020**, *109*, 110268. [[CrossRef](#)]
24. Ansari, A.A.; Aldalbahi, A.; Labis, J.P.; El-Toni, A.M.; Ahamed, M.; Manthrammel, M. Highly biocompatible, monodispersed and mesoporous $\text{La(OH)}_3\text{:Eu@mSiO}_2$ core-shell nanospheres: Synthesis and luminescent properties. *Colloids Surf. B Biointerfaces* **2018**, *163*, 133–139. [[CrossRef](#)]
25. García-Murillo, A.; Carrillo-Romo, F.D.J.; Oliva-Uc, J.; Esquivel-Castro, T.A.; de la Torre, S.D. Effects of Eu content on the luminescent properties of $\text{Y}_2\text{O}_3\text{:Eu}^{3+}$ aerogels and $\text{Y(OH)}_3\text{/Y}_2\text{O}_3\text{:Eu}^{3+}\text{@SiO}_2$ glassy aerogels. *Ceram. Int.* **2017**, *43*, 12196–12204. [[CrossRef](#)]
26. Taoufyq, A.; Mauroy, V.; Guinneton, F.; Bakiz, B.; Villain, S.; Hallaoui, A.; Benlhachemi, A.; Nolibe, G.; Lyoussi, A.; Gavarri, J.-R. Role of the chemical substitution on the luminescence properties of solid solutions $\text{Ca}(1-x)\text{Cd}(x)\text{WO}_4$ ($0 \leq x \leq 1$). *Mater. Res. Bull.* **2015**, *70*, 40–46. [[CrossRef](#)]
27. Bakiz, B.; Hallaoui, A.; Taoufyq, A.; Benlhachemi, A.; Guinneton, F.; Villain, S.; Ezahri, M.; Valmalette, J.-C.; Arab, M.; Gavarri, J.-R. Luminescent properties under X-ray excitation of $\text{Ba}(1-x)\text{Pbx}\text{WO}_4$ disordered solid solution. *J. Solid State Chem.* **2018**, *258*, 146–155. [[CrossRef](#)]
28. Hallaoui, A.; Taoufyq, A.; Arab, M.; Bakiz, B.; Benlhachemi, A.; Bazzi, L.; Villain, S.; Valmalette, J.-C.; Guinneton, F.; Gavarri, J.-R. Influence of chemical substitution on the photoluminescence of $\text{Sr}(1-x)\text{Pbx}\text{WO}_4$ solid solution. *J. Solid State Chem.* **2015**, *227*, 186–195. [[CrossRef](#)]
29. Hallaoui, A.; Taoufyq, A.; Arab, M.; Bakiz, B.; Benlhachemi, A.; Bazzi, L.; Valmalette, J.-C.; Villain, S.; Guinneton, F.; Gavarri, J.-R. Structural, vibrational and photoluminescence properties of $\text{Sr}(1-x)\text{Pbx}\text{MoO}_4$ solid solution synthesized by solid state reaction. *Mater. Res. Bull.* **2016**, *79*, 121–132. [[CrossRef](#)]
30. Xue, F.; Li, H.; Zhu, Y.; Xiong, S.; Zhang, X.; Wang, T.; Liang, X.; Qian, Y. Solvothermal synthesis and photoluminescence properties of BiPO_4 nano-cocoons and nanorods with different phases. *J. Solid State Chem.* **2009**, *182*, 1396–1400. [[CrossRef](#)]
31. Du, G.; Kan, X.; Han, Y.; Sun, Z.; Guo, W. Structure and luminescence of $\text{YPO}_4\text{:Dy}^{3+}$ microflowers. *Mater. Lett.* **2012**, *74*, 229–231. [[CrossRef](#)]
32. Yang, J.; Xiong, H.; Dong, J.; Yang, C.; Gan, S.; Zou, L. Facile hydrothermal synthesis and luminescent properties of $\text{Sm}^{3+}/\text{Eu}^{3+}$ codoped GdPO_4 phosphors. *J. Phys. Chem. Solids* **2017**, *111*, 355–363. [[CrossRef](#)]
33. Kirubanithy, M.; Irudayaraj, A.A.; Raj, A.D.; Manikandan, S. Synthesis, Characterization and Photoluminescence Behaviours of CePO_4 and Tb-doped CePO_4 Nanostructures. *Mater. Today Proc.* **2015**, *2*, 4344–4347. [[CrossRef](#)]
34. Zhang, W.; NI, Y.; Huang, W.; Lu, C.; Xu, Z. Hydrothermal synthesis, structure study and luminescent properties of $\text{YbPO}_4\text{:Tb}^{3+}$ nanoparticles. *J. Rare Earths* **2010**, *28*, 299–302. [[CrossRef](#)]
35. Bühler, G.; Feldmann, C. Microwave-Assisted Synthesis of Luminescent $\text{LaPO}_4\text{:Ce}$, Tb Nanocrystals in Ionic Liquids. *Angew. Chem. Int. Ed.* **2006**, *45*, 4864–4867. [[CrossRef](#)]
36. Bouddouch, A.; Amaterz, E.; Bakiz, B.; Taoufyq, A.; Guinneton, F.; Villain, S.; Gavarri, J.-R.; Valmalette, J.-C.; Benlhachemi, A. Customized synthesis of functional bismuth phosphate using different methods: Photocatalytic and photoluminescence properties enhancement. *Nanotechnol. Environ. Eng.* **2021**, *6*, 1–12. [[CrossRef](#)]
37. Bouddouch, A.; Amaterz, E.; Bakiz, B.; Taoufyq, A.; Guinneton, F.; Villain, S.; Valmalette, J.; Gavarri, J.; Benlhachemi, A. Photocatalytic and photoluminescence properties of CePO_4 nanostructures prepared by coprecipitation method and thermal treatment. *Optik* **2021**, *238*, 166683. [[CrossRef](#)]
38. Naciri, Y.; Hsini, A.; Bouziani, A.; Djellabi, R.; Ajmal, Z.; Laabd, M.; Navío, J.A.; Mills, A.; Bianchi, C.L.; Li, H.; et al. Photocatalytic oxidation of pollutants in gas-phase via Ag_3PO_4 -based semiconductor photocatalysts: Recent progress, new trends, and future perspectives. *Crit. Rev. Environ. Sci. Technol.* **2021**, *1*, 1–44. [[CrossRef](#)]
39. Binas, V.; Sambani, K.; Maggos, T.; Katsanaki, A.; Kiriakidis, G. Synthesis and photocatalytic activity of Mn-doped TiO_2 nanostructured powders under UV and visible light. *Appl. Catal. B Environ.* **2012**, *113–114*, 79–86. [[CrossRef](#)]
40. Zhu, Y.; Ling, Q.; Liu, Y.; Wang, H.; Zhu, Y. Photocatalytic performance of BiPO_4 nanorods adjusted via defects. *Appl. Catal. B Environ.* **2016**, *187*, 204–211. [[CrossRef](#)]
41. Pan, C.; Li, D.; Ma, X.; Chen, Y.; Zhu, Y. Effects of distortion of PO_4 tetrahedron on the photocatalytic performances of BiPO_4 . *Catal. Sci. Technol.* **2011**, *1*, 1399–1405. [[CrossRef](#)]
42. Pan, C.; Zhu, Y. A review of BiPO_4 , a highly efficient oxyacid-type photocatalyst, used for environmental applications. *Catal. Sci. Technol.* **2015**, *5*, 3071–3083. [[CrossRef](#)]

43. Zhu, Y.; Liu, Y.; Lv, Y.; Ling, Q.; Liu, D.; Zhu, Y. Enhancement of photocatalytic activity for BiPO₄ via phase junction. *J. Mater. Chem. A* **2014**, *2*, 13041–13048. [[CrossRef](#)]
44. Zhu, Y.; Wang, Y.; Ling, Q.; Zhu, Y. Enhancement of full-spectrum photocatalytic activity over BiPO₄/Bi₂WO₆ composites. *Appl. Catal. B Environ.* **2017**, *200*, 222–229. [[CrossRef](#)]
45. Zhang, Y.; Selvaraj, R.; Sillanpää, M.; Kim, Y.; Tai, C.-W. The influence of operating parameters on heterogeneous photocatalytic mineralization of phenol over BiPO₄. *Chem. Eng. J.* **2014**, *245*, 117–123. [[CrossRef](#)]
46. Zhang, Y.; Sillanpää, M.; Obregón, S.; Colón, G. A novel two-steps solvothermal synthesis of nanosized BiPO₄ with enhanced photocatalytic activity. *J. Mol. Catal. A Chem.* **2015**, *402*, 92–99. [[CrossRef](#)]
47. Liu, Y.; Zhu, Y.; Xu, J.; Bai, X.; Zong, R.; Zhu, Y. Degradation and mineralization mechanism of phenol by BiPO₄ photocatalysis assisted with H₂O₂. *Appl. Catal. B Environ.* **2013**, *142–143*, 561–567. [[CrossRef](#)]
48. Liu, G.; Liu, S.; Lu, Q.; Sun, H.; Xiu, Z. Synthesis of Mesoporous BiPO₄ Nanofibers by Electrospinning with Enhanced Photocatalytic Performances. *Ind. Eng. Chem. Res.* **2014**, *53*, 13023–13029. [[CrossRef](#)]
49. Lv, Y.; Zhu, Y.; Zhu, Y. Enhanced Photocatalytic Performance for the BiPO_{4-x} Nanorod Induced by Surface Oxygen Vacancy. *J. Phys. Chem. C* **2013**, *117*, 18520–18528. [[CrossRef](#)]
50. Lin, Y.-F.; Chang, H.-W.; Lu, S.-Y.; Liu, C.W. Preparation, Characterization, and Electrophysical Properties of Nanostructured BiPO₄ and Bi₂Se₃ Derived from a Structurally Characterized, Single-Source Precursor Bi[Se₂P(OiPr)₂]₃. *J. Phys. Chem. C* **2007**, *111*, 18538–18544. [[CrossRef](#)]
51. Li, G.; Ding, Y.; Zhang, Y.; Lu, Z.; Sun, H.; Chen, R. Microwave synthesis of BiPO₄ nanostructures and their morphology-dependent photocatalytic performances. *J. Colloid Interface Sci.* **2011**, *363*, 497–503. [[CrossRef](#)] [[PubMed](#)]
52. Geng, J.; Hou, W.-H.; Lv, Y.-N.; Zhu, J.-J.; Chen, H.-Y. One-Dimensional BiPO₄Nanorods and Two-Dimensional BiOCl Lamellae: Fast Low-Temperature Sonochemical Synthesis, Characterization, and Growth Mechanism. *Inorg. Chem.* **2005**, *44*, 8503–8509. [[CrossRef](#)] [[PubMed](#)]
53. Pan, C.; Xu, J.; Chen, Y.; Zhu, Y. Influence of OH-related defects on the performances of BiPO₄ photocatalyst for the degradation of rhodamine B. *Appl. Catal. B Environ.* **2012**, *115–116*, 314–319. [[CrossRef](#)]
54. Pan, C.; Zhu, Y. New Type of BiPO₄ Oxy-Acid Salt Photocatalyst with High Photocatalytic Activity on Degradation of Dye. *Environ. Sci. Technol.* **2010**, *44*, 5570–5574. [[CrossRef](#)]
55. Becerro, A.I.; Criado, J.; Gontard, L.C.; Obregón, S.; Fernández, A.; Colón, G.; Ocaña, M. Bifunctional, Monodisperse BiPO₄-Based Nanostars: Photocatalytic Activity and Luminescent Applications. *Cryst. Growth Des.* **2014**, *14*, 3319–3326. [[CrossRef](#)]
56. Yan-Yan, Z.; Yan-Fang, L.; Yan-Hui, L.; Hua, W.; Qiang, L.; Yong-Fa, Z. Reflux Preparation and Photocatalytic Performance of Bismuth Phosphate Nanorods. *Acta Phys.-Chim. Sin.* **2013**, *29*, 576–584. [[CrossRef](#)]
57. Zhang, Q.; Tian, H.; Li, N.; Chen, M.; Teng, F. Controllable growth of novel BiPO₄ dendrites by an innovative approach and high energy facets-dependent photocatalytic activity. *CrystEngComm* **2014**, *16*, 8334–8339. [[CrossRef](#)]
58. Li, L.; Xu, J.; Guo, C.; Zhang, Y. Removal of rhodamine B from aqueous solution by BiPO₄ hierarchical architecture. *Front. Environ. Sci. Eng.* **2013**, *7*, 382–387. [[CrossRef](#)]
59. Ye, H.; Lin, H.; Cao, J.; Chen, S.; Chen, Y. Enhanced visible light photocatalytic activity and mechanism of BiPO₄ nanorods modified with AgI nanoparticles. *J. Mol. Catal. A Chem.* **2014**, *397*, 85–92. [[CrossRef](#)]
60. Cheng, L.-W.; Tsai, J.-C.; Huang, T.-Y.; Huang, C.-W.; Unnikrishnan, B.; Lin, Y.-W. Controlled synthesis, characterization and photocatalytic activity of BiPO₄ nanostructures with different morphologies. *Mater. Res. Express* **2014**, *1*. [[CrossRef](#)]
61. Bouddouch, A.; Amaterz, E.; Bakiz, B.; Taoufyq, A.; Guinneton, F.; Villain, S.; Gavarri, J.; Ezahri, M.; Valmalette, J.; Benlhachemi, A. Role of thermal decomposition process in the photocatalytic or photoluminescence properties of BiPO₄ polymorphs. *Water Environ. Res.* **2020**, *92*, 1874–1887. [[CrossRef](#)]
62. Zhao, M.; Yang, L.; Li, G.; Li, L.; Zheng, J. Exploring the unique electrical properties of metastable BiPO₄ through switchable phase transitions. *CrystEngComm* **2013**, *15*, 609–615. [[CrossRef](#)]
63. Poloznikova, M.E.; Fomichev, V.V. The vibrational spectra and characteristic features of the orthophosphates of Group I–III elements. *Russ. Chem. Rev.* **1994**, *63*, 399–409. [[CrossRef](#)]
64. Silva, E.; Ayala, A.P.; Guedes, I.; Paschoal, C.; Moreira, R.; Loong, C.-K.; Boatner, L. Vibrational spectra of monazite-type rare-earth orthophosphates. *Opt. Mater.* **2006**, *29*, 224–230. [[CrossRef](#)]
65. Heuser, J.; Bukaemskiy, A.; Neumeier, S.; Neumann, A.; Bosbach, D. Raman and infrared spectroscopy of monazite-type ceramics used for nuclear waste conditioning. *Prog. Nucl. Energy* **2014**, *72*, 149–155. [[CrossRef](#)]
66. Yang, L.-Y.; Dong, S.-Y.; Sun, J.-H.; Feng, J.-L.; Wu, Q.-H.; Sun, S.-P. Microwave-assisted preparation, characterization and photocatalytic properties of a dumbbell-shaped ZnO photocatalyst. *J. Hazard. Mater.* **2010**, *179*, 438–443. [[CrossRef](#)] [[PubMed](#)]
67. McLaren, A.; Valdes-Solis, T.; Li, G.; Tsang, S.C. Shape and Size Effects of ZnO Nanocrystals on Photocatalytic Activity. *J. Am. Chem. Soc.* **2009**, *131*, 12540–12541. [[CrossRef](#)]
68. Wang, Y.; Li, X.; Wang, N.; Quan, X.; Chen, Y. Controllable synthesis of ZnO nanoflowers and their morphology-dependent photocatalytic activities. *Sep. Purif. Technol.* **2008**, *62*, 727–732. [[CrossRef](#)]